Downloaded from orbit.dtu.dk on: Aug 25, 2022

DTU Library

Intermodal and cross-polarization four-wave mixing in large-core hybrid photonic crystal fibers

Petersen, Sidsel Rübner; Alkeskjold, Thomas Tanggaard; Olausson, Christina Bjarnal Thulin; Lægsgaard, Jesper

Published in:
Optics Express

Link to article, DOI:
10.1364/OE.23.5954

Publication date:
2015

Document Version
Publisher's PDF, also known as Version of record

Link back to DTU Orbit

Citation (APA):
Petersen, S. R., Alkeskjold, T. T., Olausson, C. B. T., & Lægsgaard, J. (2015). Intermodal and cross-polarization four-wave mixing in large-core hybrid photonic crystal fibers. *Optics Express*, *23*(5), 5954-5971. https://doi.org/10.1364/OE.23.5954

General rights
Copyright and moral rights for the publications made accessible in the public portal are retained by the authors and/or other copyright owners and it is a condition of accessing publications that users recognise and abide by the legal requirements associated with these rights.

- Users may download and print one copy of any publication from the public portal for the purpose of private study or research.
- You may not further distribute the material or use it for any profit-making activity or commercial gain
- You may freely distribute the URL identifying the publication in the public portal

If you believe that this document breaches copyright please contact us providing details, and we will remove access to the work immediately and investigate your claim.

Intermodal and cross-polarization four-wave mixing in large-core hybrid photonic crystal fibers

Sidsel R. Petersen,[1,*] Thomas T. Alkeskjold,[2] Christina B. Olausson,[2] and Jesper Lægsgaard[1]

[1]*DTU Fotonik, Department of Photonics Engineering, Technical University of Denmark, 2800 Kgs. Lyngby, Denmark*

[2]*NKT Photonics A/S, Blokken 84, 3460 Birkerød, Denmark*

[*]*srpe@fotonik.dtu.dk*

Abstract: Degenerate four-wave mixing is considered in large mode area hybrid photonic crystal fibers, combining photonic bandgap guidance and index guidance. Co- and orthogonally polarized pump, signal and idler fields are considered numerically by calculating the parametric gain and experimentally by spontaneous degenerate four-wave mixing. Intermodal and birefringence assisted intramodal phase matching is observed. Good agreement between calculations and experimental observations is obtained. Intermodal four-wave mixing is achieved experimentally with a conversion efficiency of 17 %.

© 2015 Optical Society of America

OCIS codes: (060.5295) Photonic crystal fibers; (060.4370) Nonlinear optics, fibers; (190.4380) Nonlinear optics, four-wave mixing.

References and links

1. J. D. Harvey, R. Leonhardt, S. Coen, G. K. L. Wong, J. C. Knight, W. J. Wadsworth, and P. St. J. Russell, "Scalar modulation instability in the normal dispersion regime by use of a photonic crystal fiber," Opt. Lett. **28**(22), 2225–2227 (2003).
2. S. R. Petersen, T. T. Alkeskjold, and J. Lægsgaard, "Degenerate four wave mixing in large mode area hybrid photonic crystal fibers," Opt. Express **21**(15), 18111–18124 (2013).
3. S. R. Petersen, T. T. Alkeskjold, C. B. Olausson, and J. Lægsgaard, "Extended parametric gain range in photonic crystal fibers with strongly frequency-dependent field distributions," Opt. Lett. **39**(16), 4891–4894 (2014).
4. P. D. Rasmussen, J. Lægsgaard, and O. Bang, "Degenerate four wave mixing in solid core photonic bandgap fibers," Opt. Express **16**(6), 4059–4068 (2008).
5. A. Cerqueira S. Jr, J. M. Chavez Boggio, H. E. Hernandez-Figueroa, H. L. Fragnito, and J. C. Knight, "Highly efficient generation of cascaded Four-Wave Mixing products in a Hybrid Photonic Crystal Fiber," in Proc. of European Conference on Optical Communication (ECOC 2007).
6. J. Zhao, P. Yan, J. Shu, C. Du, S. Ruan, H. Wei, and J. Luo, "Efficient anti-stokes signal generation through degenerate four wave mixing in an all solid photonic bandgap fiber," Opt. Commun. **284**(21), 5208–5211 (2011).
7. R. T. Murray, E. J. R. Kelleher, S. V. Popov, A. Mussot, A. Kudlinski, and J. R. Taylor "Widely tunable polarization maintaining photonic crystal fiber based parametric wavelength conversion," Opt. Express **21**(13), 15826–15833 (2013).
8. E. A. Zlobina, S. I. Kablukov, and S. A. Babi, "Phase matching for parametric generation in polarization maintaining photonic crystal fiber pumped by tunable Yb-doped fiber laser," J. Opt. Soc. Am. B **29**(8), 1959–1967 (2012).
9. J. Yuan, G. Zhou, H. Liu, C. Xia, X. Sang, Q. Wu, C. Yu, K. Wang, B. Yan, Y. Han, G. Farrell, and L. Hou, "Coherent anti-stokes raman scattering microscopy by dispersive wave generations in a polarization maintaining photonic crystal fiber," Pr. Electromagn. Res. **141**, 659–670 (2013).
10. S. R. Petersen, T. T. Alkeskjold, C. B. Olausson, and J. Lægsgaard, "Polarization switch of four-wave mixing in large mode area hybrid photonic crystal fibers," Opt. Lett. **40**(4), 487–490 (2015).

#231607 - $15.00 USD Received 29 Dec 2014; revised 16 Feb 2015; accepted 17 Feb 2015; published 25 Feb 2015
© 2015 OSA

11. R. H. Stolen, J. E. Bjorkholm, and A. Ashkin, "Phase-matched three-wave mixing in silica fiber optical waveguides," Appl. Phys. Lett. **24**(7), 308–310 (1974).
12. R. H. Stolen, "Phase-matched-stimulated four-photon mixing in silica-fiber waveguides," IEEE J. Quantum Elect. **11**(3), 100–103 (1975).
13. P. Steinvurzel, J. Demas, B. Tai, Y. Chen, L. Yan, and S. Ramachandran, "Broadband parametric wavelength conversion at 1 μm with large mode area fibers," Opt. Lett. **39**(4), 743–746 (2014).
14. E. Coscelli, F. Poli, T. T. Alkeskjold, D. Passaro, A. Cucinotta, L. Leick, J. Broeng, and S. Selleri, "Single-mode analysis of Yb-doped double-cladding distributed spectral filtering photonic crystal fibers," Opt. Express **18**(26), 27197–27204 (2010).
15. S. R. Petersen, T. T. Alkeskjold, F. Poli, E. Coscelli, M. M. Jørgensen, M. Laurila, J. Lægsgaard, and J. Broeng, "Hybrid Ytterbium-doped large-mode-area photonic crystal fiber amplifier for long wavelengths," Opt. Express **20**(6), 6010–6020 (2012).
16. T. T. Alkeskjold, "Large-mode-area ytterbium-doped fiber amplifier with distributed narrow spectral filtering and reduced bend sensitivity," Opt. Express **17**(19), 16394–16405 (2009).
17. A. Argyros, T. A. Birks, S. G. Leon-Saval, C. M. B. Cordeiro, and P. St.J. Russell, "Guidance properties of low-contrast photonic bandgap fibres," Opt. Express **13**(7), 2503–2511 (2005).
18. S. C. Rashleigh, "Measurement of fiber birefringence by wavelength scanning: effect of dispersion," Opt. Lett. **8**(6), 336–338 (1983).
19. COMSOL Multiphysics, version 4.4, www.comsol.com.
20. J. K. Lyngsø, B. J. Mangan, C. B. Olausson, and P. J. Roberts, "Stress induced birefringence in hybrid TIR/PBG guiding solid photonic crystal fibers," Opt. Express **18**(13), 14031–14040 (2010).
21. G. P. Agrawal, *Nonlinear Fiber Optics*, IV edition, (Elsevier, 2007).
22. M. E. Marhic, K. K. Y. Wong, and L. G. Kazovsky, "Fiber optical parametric amplifiers with linearly or circularly polarized waves," J. Opt. Soc. Am. B **20**(12), 2425–2433 (2003).
23. D. Milam, "Review and assessment of measured values of the nonlinear refractive-index coefficient of fused silica," App. Opt. **37**(3), 546–550 (1998).

1. Introduction

Rare-earth doped fiber lasers and amplifiers are undergoing rapid development, and several efforts have been made to utilize the full spectral potential of the emission cross sections of the available rare-earth dopants. However, there exist spectral regions where no emission of rare-earth dopants is available, and thus they are insufficient to cover the full optical spectrum. To achieve full spectral coverage different mechanisms must be considered, and one approach is to utilize the nonlinear response of silica.

Four-wave mixing (FWM) in silica fibers can be used to convert optical output frequencies from those easily achievable with rare-earth doped fiber lasers to frequencies that are less accessible. FWM requires phase matching; thus, fiber dispersion properties are crucial. The two contributions to fiber dispersion are material and waveguide dispersion. The material dispersion of silica is intrinsic; therefore, only the waveguide dispersion is useful in tailoring the fiber dispersion. Sufficiently large waveguide dispersion can be achieved by confining the fiber mode very tightly, as in for example photonic crystal fibers (PCFs) [1]. However, large mode area (LMA) fiber designs are necessary for power scaling, and material dispersion often becomes the dominant contribution for larger core sizes.

There is a growing interest in FWM in photonic bandgap (PBG) guiding fibers [2–6]. Fiber modes near the PBG edges are strongly affected by waveguide dispersion, thus the PBG effect can be used to tailor fiber dispersion, even in LMA fibers. Birefringence-assisted FWM in polarization maintaining (PM) PCFs has also been investigated [7–9]. Phase matching relies on the different phase velocities of the waves propagating in the two polarization modes of a PM PCF. This method can also be applied to achieve control of the phase matching in LMA fibers, which was recently demonstrated [10]. Intermodal FWM has been known for many years [11, 12], and it has also been proposed for phase matching in LMA fibers [13]. In multimode fibers each mode has distinct dispersion properties, and phase matching can be achieved by choosing the modes with appropriate dispersion in the FWM process.

In this work we consider FWM in a LMA hybrid PCF with a core diameter of 36 μm, where

#231607 - $15.00 USD Received 29 Dec 2014; revised 16 Feb 2015; accepted 17 Feb 2015; published 25 Feb 2015
© 2015 OSA

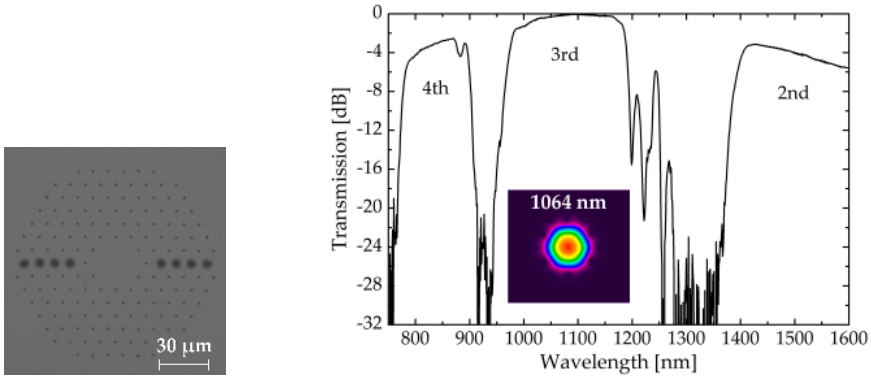

(a) (b)

Fig. 1. **(a)** Microscope image of the hybrid photonic crystal fiber. The small dark features indicate the location of the airholes, while the larger dark features indicate the location of the Germanium-doped silica rods. **(b)** White light transmission spectrum through a 6 m length of hybrid photonic crystal fiber. The 2nd, 3rd, and 4th bandgaps are observed. The inset shows an image of the output of 1064 nm launched in the core of the hybrid photonic crystal fiber.

index-guiding and guidance through the PBG effect are simultaneously present and different phase matching mechanisms are utilized. Fiber birefringence gives rise to intramodal FWM in the same transmission band as that of the pump laser. Intermodal FWM across transmission bands is also observed, where phase matching is achieved for modes having dispersion properties which are both affected and unaffected by the waveguide dispersion arising from the PBG effect. Various phase matching techniques in hybrid PCFs provide control of the generated spectral components in a FWM process, demonstrating that FWM in a LMA hybrid PCF is a viable method by which it is possible to increase the spectral coverage of high power fiber lasers and amplifiers.

2. Hybrid photonic crystal fibers

In Fig. 1(a) a microscope image of the cross section of the LMA hybrid PCF considered in this work is shown. The cladding consists of airholes positioned in a hexagonal lattice with a hole-to-hole spacing of 9.3 µm and an airhole diameter of 1.6 µm. Seven missing airholes define the core area, which has a diameter of 36 µm. Eight of the airholes are replaced by high-index Germanium-doped silica rods (Ge-rods) with a diameter of 6.6 µm and numerical aperture of 0.29. The diameter of the fiber is 437 µm, not taking the polymer coating into account.

The combination of airholes and Ge-rods in the hybrid PCF gives rise to two different guiding mechanisms; the core modes are confined by index-guiding caused by the airholes and by the photonic bandgap effect arising from the presence of the high-index Ge-rods. The number of modes guided by the core can be controlled through the airhole diameter, while the spectral position of the transmission band is controlled by the Ge-rod diameter [14–16].

2.1. Measured fiber properties

In Fig. 1(b) a spectrum of unpolarized white light transmitted through a 6 m section of hybrid PCF coiled with a diameter of 50 cm is shown. Three transmission bands are observed, one band ranging from 775 nm to 900 nm, a second band ranging from 975 nm to 1200 nm, and a third band starting at 1400 nm. These observed transmission bands correspond to the 4th,

#231607 - $15.00 USD Received 29 Dec 2014; revised 16 Feb 2015; accepted 17 Feb 2015; published 25 Feb 2015
© 2015 OSA

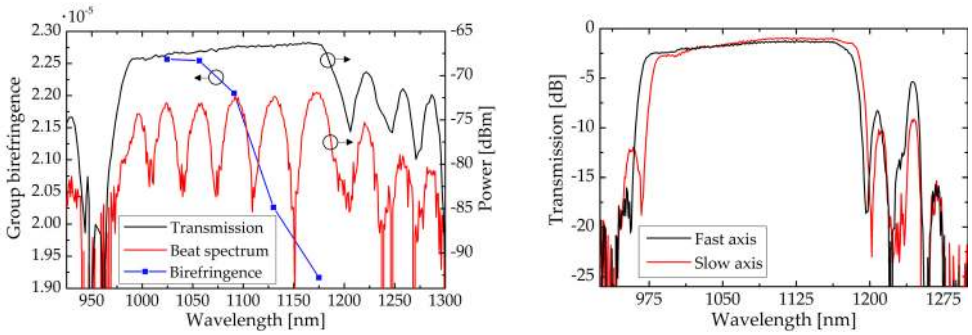

(a) (b)

Fig. 2. **(a)** Measurement of the group birefringence in a 1.5 m length of hybrid photonic crystal fiber using the scanning wavelength method. **(b)** White light transmission measurement of light polarized along the slow and the fast axis in a 6 m length of hybrid PCF.

3rd, and 2nd bandgaps, respectively, with the numbering corresponding to standard notation in PBG fibers [17]. Furthermore, an image of the hybrid PCF output for a launched wavelength of 1064 nm is shown in the inset of Fig. 1(b).

The twofold symmetry of the hybrid PCF gives rise to birefringence. The fiber has two principal axes; the slow axis oriented in the direction along the Ge-rods, and the fast axis oriented in the direction orthogonal to the Ge-rods. The total birefringence is given by the geometrical birefringence and the stress induced birefringence. The stress induced birefringence is generated during the fabrication process of the fiber, caused by the differences in the thermal expansion coefficients of Ge-rods and pure silica. The stress distribution is non-symmetric in the fiber core, since the Ge-rods are only present along one axis of the fiber, resulting in stress induced birefringence. The stress induced birefringence is substantially larger than the geometrical birefringence in the hybrid PCF.

In Fig. 2(a) a measurement of the group birefringence in a 1.5 m length of the hybrid PCF coiled with a diameter of 30 cm using the scanning wavelength method is shown [18]. Polarized white light is launched in the fiber core with a polarization angle of 45° with respect to the principal axes of the fiber. The output is collected through a polarizer which also has an angle of 45° with respect to the principal axes of the fiber. The resulting beat spectrum is shown in Fig. 2(a), and has a period characteristic of the difference in propagation constants of the two principal axes and the given fiber length. An unpolarized white light transmission measurement in the hybrid PCF is also shown, to indicate the values of group birefringence with respect to the transmission band edges. The group birefringence is larger than 2×10^{-5} in the spectral range 1025 nm - 1130 nm.

Birefringence also impacts the transmission bands of the fiber. In Fig. 2(b) a white light transmission measurement of light polarized along the slow and fast axes in a 6 m length of hybrid PCF coiled with a diameter of 50 cm is shown. The transmission band is slightly red shifted when the polarization is oriented along the slow axis. At 975 nm the transmission band edge for the slow axis is red shifted by 12 nm as compared to the transmission band edge for the fast axis.

2.2. *Calculated fiber properties*

Properties of the hybrid PCF are also considered numerically. The propagation constants and field distributions of the modes in the hybrid PCF are calculated with a full-vector modal solver

#231607 - $15.00 USD Received 29 Dec 2014; revised 16 Feb 2015; accepted 17 Feb 2015; published 25 Feb 2015
© 2015 OSA

Table 1. Physical values used in the calculation of the stress birefringence.

Material property	Value
Young's modulus	72 GPa
Poisson's ratio	0.17
First stress-optical coefficient	$0.65 \times 10^{-12}\,\mathrm{m^2/N}$
Second stress-optical coefficient	$4.2 \times 10^{-12}\,\mathrm{m^2/N}$
Operating temperature	20 °C
Reference temperature	1050 K

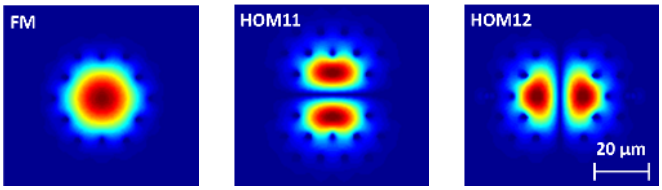

(a) (b) (c)

Fig. 3. Calculated field distributions of the fundamental mode (FM) and the two orientations of the LP_{11} mode for the modes polarized along the slow axis at 1064 nm.

based on the finite element method [19]. The values used for airhole- and fiber diameter in the calculations are identical to those of the fabricated fiber, but the Ge-rod diameter has been increased by 6 % in the calculation to obtain a better agreement between calculated and measured transmission properties. The discrepancies between the calculated and measured transmission properties are probably due to the uncertainties of the physical values of the refractive indices and dimensions in the fabricated fiber. The refractive index of the Ge-rods is approximated with a staircase function [14].

The stress birefringence, induced by thermal expansions during the fabrication process of the fiber, has to be taken into account in the calculation to achieve correct properties for the modes polarized along the slow and fast axis. This stress birefringence is determined using a plane strain approximation, assuming that the strain along the longitudinal fiber direction is zero. The local anisotropic refractive index is thus given by $n_i = n_0 - C_1\sigma_i - C_2(\sigma_j + \sigma_k)$, where σ_x, σ_y, and σ_z are the calculated stress distributions of the fiber cross section, n_0 is the refractive index of the unstressed material, C_1 and C_2 are the first and second stress-optical coefficients, respectively, and i, j, k is a cyclic permutation of x, y, z. The stress induced birefringence is calculated with the 2D Solid Mechanics interface in [19]. The mechanical and optical properties used in the stress birefringence calculations are shown in Table 1. The properties shown correspond to those of pure silica and are applied identically to the Ge-doped silica regions, which is in agreement with approximations used in previous calculations of thermally induced stress birefringence [20]. Stress birefringence arises purely from the difference in the thermal expansion coefficients in the calculation, which are set to $0.4 \times 10^{-6}\,1/\mathrm{K}$ and $1.7 \times 10^{-6}\,1/\mathrm{K}$ for silica and the Ge-rods respectively.

The fundamental mode (FM) and LP_{11} modes are considered in the calculations. The calculated field distributions for the modes at 1064 nm are shown in Fig. 3. The LP_{11} mode with a minimum in the field distribution along the slow axis is labeled HOM11, see Fig. 3(b), while the LP_{11} mode with a minimum along the fast axis is labeled HOM12, see Fig. 3(c). For each of the modes in Figs. 3(a)–3(c) the polarization along the slow and fast axis will be considered.

#231607 - $15.00 USD Received 29 Dec 2014; revised 16 Feb 2015; accepted 17 Feb 2015; published 25 Feb 2015
© 2015 OSA

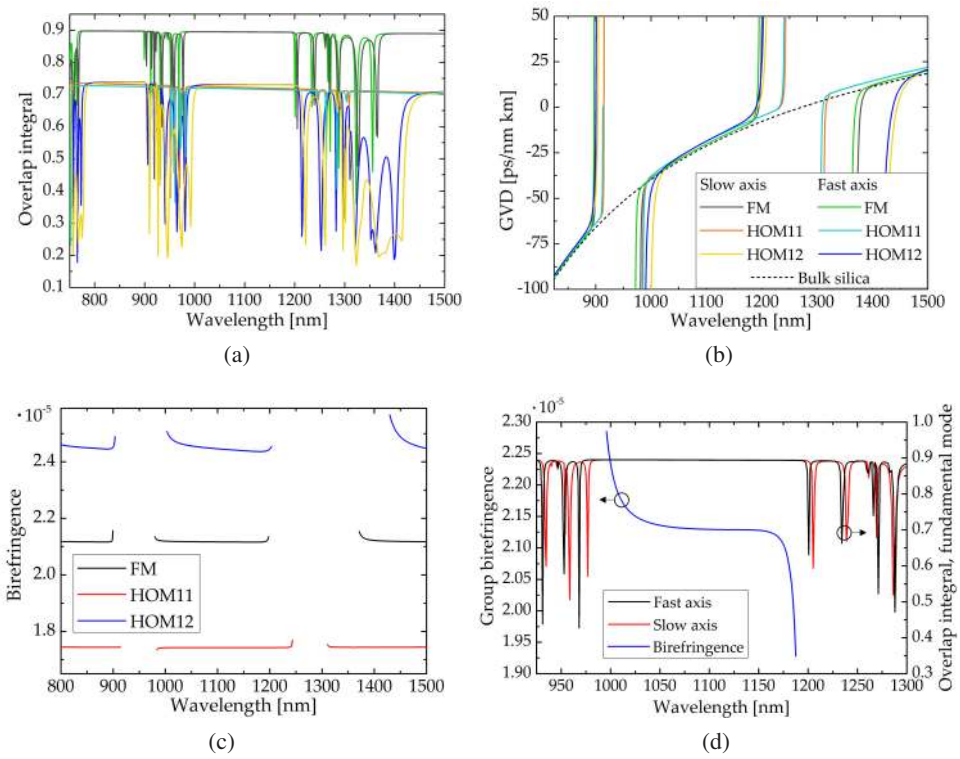

Fig. 4. **(a)** Calculated overlap integral of the fundamental mode and two orientations of the LP_{11} modes with the core region. The polarization along the slow and fast axis are considered. The LP_{11} modes are labeled according to Fig. 3. The legend in Fig. 4(b) also applies to Fig. 4(a). **(b)** Calculated group velocity dispersion (GVD) of the fundamental mode and two orientations of the LP_{11} modes. The polarization along the slow and fast axis are considered. **(c)** Calculated birefringence, $n_{\mathrm{eff,s}} - n_{\mathrm{eff,f}}$, of the fundamental mode and two orientations of the LP_{11} modes. **(d)** Calculated group birefringence, $n_{\mathrm{gs}} - n_{\mathrm{gf}}$, and overlap integral with the core region of the fundamental mode polarized along the slow and fast axis.

The calculated overlap integrals of the FM and LP_{11} modes with the core region are shown in Fig. 4(a). Large values of overlap integral in a wide spectral range can be interpreted as a transmission band. When several closely-spaced dips in the overlap integral values are observed in a spectral region, the region falls outside a transmission band and optical confinement in the core is not expected. Three transmission bands are observed for the FM in the considered spectral region, one band ranging from 770 nm to 900 nm, a second band ranging from 975 nm to 1200 nm, and a third with the blue edge of the transmission band at 1370 nm, all of which is in good agreement with experimental results. Three transmission bands are also observed for the LP_{11} modes, however, the overlap integral values of the LP_{11} modes are lower than for the FM. For the FM the values are close to 0.9 in the transmission bands, while for the LP_{11} modes the values are closer to 0.7. HOM content is therefore expected in the hybrid PCF, but the LP_{11} mode will experience a higher loss than the FM due to lower confinement.

The calculated group velocity dispersion (GVD) is shown in Fig. 4(b). The group velocity dispersion of bulk silica is also shown in the figure for reference, which is calculated from the Sellmeier equation of fused silica. The GVD is very similar to that of bulk silica in the

#231607 - $15.00 USD Received 29 Dec 2014; revised 16 Feb 2015; accepted 17 Feb 2015; published 25 Feb 2015
© 2015 OSA

transmission bands of the hybrid PCF, but near the transmission band edges the GVD diverges substantially, and large values of normal and anomalous dispersion are present. This behavior is related to the guiding properties of the hybrid PCF. Within a transmission band the core mode is well confined and material dispersion dominates. Waveguide dispersion is the dominant contribution to the GVD near the band edges, and the GVD is thus very different from that of bulk silica.

The calculated mode birefringence given by the effective refractive index along the slow axis, $n_{\mathrm{eff,s}}$, minus the effective refractive index along the fast axis, $n_{\mathrm{eff,f}}$, is shown in Fig. 4(c) for the FM and LP_{11} modes. The thermally induced stress birefringence is largest in the proximity of the Ge-rods. HOM12 is thus affected by the thermally induced stress to a larger degree than HOM11 due to the different field distributions.

Calculated group birefringence of the FM, given by the group index along the slow axis, n_{gs}, minus the group index along the fast axis, n_{gf}, is shown in Fig. 4(d). The reference temperature stated in Table 1 was chosen to achieve a reasonable match between the measured and calculated group birefringence. Furthermore, the FM transmission band from approximately 975 nm to 1200 nm is shown for both polarizations. The transmission band of the slow axis is red shifted compared to the transmission band of the fast axis; at 975 nm the transmission band edge is shifted by 9 nm. Similar behaviour is observed in the experimental and calculated group birefringence, see Figs. 2 and 4(d). The group birefringence has the highest values for shorter wavelengths and decreases for longer wavelengths. Furthermore a similar spectral red shift of the transmission band for light polarized along the slow axis compared to the transmission band for light polarized along the fast axis is observed both in the measurement and in the calculation.

In the following a pump laser with a wavelength of 1064 nm will be considered in the FWM processes. According to Fig. 4(b) the GVD at 1064 nm is $-26\,\mathrm{ps}/(\mathrm{nm{\cdot}km})$ for both polarizations of the FM, and the pump wavelength is thus located within the normal dispersion regime. The birefringence for the FM is 2.12×10^{-5} at 1064 nm.

3. Four wave mixing theory

In a degenerate FWM process two pump photons of equal frequency are annihilated and signal and idler photons are generated. Energy conservation has to be fulfilled, which can be stated through the relation $2\omega_1=\omega_2+\omega_3$, where ω_1, ω_2 and ω_3 are the angular frequencies of the pump, signal and idler fields, respectively. Furthermore the phase matching condition must also be fulfilled. Phase matching contributions arise from both linear and nonlinear dispersion, where the linear contribution is given by: $\Delta\beta=\beta_2+\beta_3-2\beta_1$, where β_2, β_3, and β_1 are the propagation constants for the signal, idler, and pump fields, respectively, and the nonlinear contribution arises from the Kerr effect.

The parametric gain of a FWM process can be derived from the wave equation. Assuming that the process occurs in a non-magnetic isotropic medium with no free charges or currents, the wave equation for the electric field, $\mathbf{E}$, can be expressed in terms of the nonlinear polarization, $\mathbf{P}_{NL}$, [21]:

$$\nabla^2\mathbf{E}-\frac{n^2}{c^2}\frac{\partial\mathbf{E}}{\partial t}=\mu_0\frac{\partial^2\mathbf{P}_{NL}}{\partial t^2}\,, \tag{1}$$

where n is the linear refractive index, c is the speed of light, and μ_0 is the vacuum permeability.

#231607 - $15.00 USD Received 29 Dec 2014; revised 16 Feb 2015; accepted 17 Feb 2015; published 25 Feb 2015
© 2015 OSA

For a degenerate FWM process $\mathbf{E}$ and $\mathbf{P}_{NL}$ can be decomposed as:

$$\mathbf{E} = \frac{1}{2}\sum_{j=1}^{3}\left[\mathbf{E}_j e^{-i\omega_j t} + \mathbf{E}_j^* e^{i\omega_j t}\right] , \tag{2}$$

$$\mathbf{P}_{\mathrm{NL}} = \frac{1}{2}\sum_{j=1}^{3}\left[\mathbf{P}_j e^{-i\omega_j t} + \mathbf{P}_j^* e^{i\omega_j t}\right] . \tag{3}$$

The nonlinear polarization can be written as, [22]:

$$\mathbf{P}_{\mathrm{NL}} = \varepsilon_0 \chi^{(3)}_{xxxx}(\mathbf{E}\cdot\mathbf{E})\mathbf{E} . \tag{4}$$

By combining Eqs. (2) and (4) a complete expression for the nonlinear polarization can be obtained. This is a rather comprehensive expression with 6^3 terms. To evaluate the equations for the pump, signal and idler fields, only the terms oscillating at the pump, signal and idler frequencies must be considered:

$$\begin{aligned}\mathbf{P}_1 =& \frac{1}{4}\varepsilon_0\chi^{(3)}_{xxxx}\Big((\mathbf{E}_1\cdot\mathbf{E}_1)\mathbf{E}_1^* + 2(\mathbf{E}_1^*\cdot\mathbf{E}_1)\mathbf{E}_1 + 2(\mathbf{E}_2^*\cdot\mathbf{E}_2)\mathbf{E}_1 + 2(\mathbf{E}_3^*\cdot\mathbf{E}_3)\mathbf{E}_1 \\ &+ 2(\mathbf{E}_2^*\cdot\mathbf{E}_1)\mathbf{E}_2 + 2(\mathbf{E}_3^*\cdot\mathbf{E}_1)\mathbf{E}_3 + 2(\mathbf{E}_2\cdot\mathbf{E}_1)\mathbf{E}_2^* + 2(\mathbf{E}_3\cdot\mathbf{E}_1)\mathbf{E}_3^* + \\ &2(\mathbf{E}_3\cdot\mathbf{E}_1^*)\mathbf{E}_2 + 2(\mathbf{E}_2\cdot\mathbf{E}_1^*)\mathbf{E}_3 + 2(\mathbf{E}_2\cdot\mathbf{E}_3)\mathbf{E}_1^*\Big) ,\end{aligned} \tag{5}$$

$$\begin{aligned}\mathbf{P}_2 =& \frac{1}{4}\varepsilon_0\chi^{(3)}_{xxxx}\Big((\mathbf{E}_2\cdot\mathbf{E}_2)\mathbf{E}_2^* + 2(\mathbf{E}_2^*\cdot\mathbf{E}_2)\mathbf{E}_2 + 2(\mathbf{E}_1^*\cdot\mathbf{E}_1)\mathbf{E}_2 + 2(\mathbf{E}_3^*\cdot\mathbf{E}_3)\mathbf{E}_2 + 2(\mathbf{E}_1^*\cdot\mathbf{E}_2)\mathbf{E}_1 \\ &+ 2(\mathbf{E}_3^*\cdot\mathbf{E}_2)\mathbf{E}_3 + 2(\mathbf{E}_1\cdot\mathbf{E}_2)\mathbf{E}_1^* + 2(\mathbf{E}_3\cdot\mathbf{E}_2)\mathbf{E}_3^* + 2(\mathbf{E}_1\cdot\mathbf{E}_3^*)\mathbf{E}_1 + (\mathbf{E}_1\cdot\mathbf{E}_1)\mathbf{E}_3^*\Big) ,\end{aligned} \tag{6}$$

$$\begin{aligned}\mathbf{P}_3 =& \frac{1}{4}\varepsilon_0\chi^{(3)}_{xxxx}\Big((\mathbf{E}_3\cdot\mathbf{E}_3)\mathbf{E}_3^* + 2(\mathbf{E}_3^*\cdot\mathbf{E}_3)\mathbf{E}_3 + 2(\mathbf{E}_1^*\cdot\mathbf{E}_1)\mathbf{E}_3 + 2(\mathbf{E}_2^*\cdot\mathbf{E}_2)\mathbf{E}_3 + 2(\mathbf{E}_1^*\cdot\mathbf{E}_3)\mathbf{E}_1 \\ &+ 2(\mathbf{E}_2^*\cdot\mathbf{E}_3)\mathbf{E}_2 + 2(\mathbf{E}_1\cdot\mathbf{E}_3)\mathbf{E}_1^* + 2(\mathbf{E}_2\cdot\mathbf{E}_3)\mathbf{E}_2^* + 2(\mathbf{E}_1\cdot\mathbf{E}_2^*)\mathbf{E}_1 + (\mathbf{E}_1\cdot\mathbf{E}_1)\mathbf{E}_2^*\Big) .\end{aligned} \tag{7}$$

In the undepleted pump approximation, it is assumed that the pump field is much stronger than the signal and idler field. Eqs. (5)-(7) can be simplified in this approximation, since several of the terms become negligible compared to terms including the square or greater of the magnitude of the pump wave field. The expressions of Eqs. (5)-(7) reduce to:

$$\mathbf{P}_1 = \frac{1}{4}\varepsilon_0\chi^{(3)}_{xxxx}\Big((\mathbf{E}_1\cdot\mathbf{E}_1)\mathbf{E}_1^* + 2(\mathbf{E}_1^*\cdot\mathbf{E}_1)\mathbf{E}_1\Big) , \tag{8}$$

$$\mathbf{P}_2 = \frac{1}{2}\varepsilon_0\chi^{(3)}_{xxxx}\Big((\mathbf{E}_1^*\cdot\mathbf{E}_1)\mathbf{E}_2 + (\mathbf{E}_1^*\cdot\mathbf{E}_2)\mathbf{E}_1 + (\mathbf{E}_1\cdot\mathbf{E}_2)\mathbf{E}_1^* + (\mathbf{E}_1\cdot\mathbf{E}_3^*)\mathbf{E}_1 + \frac{1}{2}(\mathbf{E}_1\cdot\mathbf{E}_1)\mathbf{E}_3^*\Big) , \tag{9}$$

$$\mathbf{P}_3 = \frac{1}{2}\varepsilon_0\chi^{(3)}_{xxxx}\Big((\mathbf{E}_1^*\cdot\mathbf{E}_1)\mathbf{E}_3 + (\mathbf{E}_1^*\cdot\mathbf{E}_3)\mathbf{E}_1 + (\mathbf{E}_1\cdot\mathbf{E}_3)\mathbf{E}_1^* + (\mathbf{E}_1\cdot\mathbf{E}_2^*)\mathbf{E}_1 + \frac{1}{2}(\mathbf{E}_1\cdot\mathbf{E}_1)\mathbf{E}_2^*\Big) . \tag{10}$$

The fields, $\mathbf{E}_j$, can be represented in terms of their Jones vectors, $\mathbf{A}_j(z)$, to account for polarization effects. The Jones vector is a two-dimensional column vector representing the components of the electric field in the $x-y$ plane. $\mathbf{E}_j$ can be written as:

$$\mathbf{E}_j = F_j(x,y)\mathbf{A}_j(z)e^{i\beta_j z} \equiv F_j(x,y)\mathbf{A}_j e^{i\beta_j z} , \tag{11}$$

where $F_j(x,y)$ represents the fiber mode profile in the transverse plane, and in the following $\mathbf{A}_j$ is implicitly assumed to depend on z. It is often assumed that the mode profiles are nearly the same for all considered fields, leading to the assumption of the same effective mode area for all

#231607 - $15.00 USD Received 29 Dec 2014; revised 16 Feb 2015; accepted 17 Feb 2015; published 25 Feb 2015
© 2015 OSA

fields. This approximation is not valid for fibers with frequency-dependent field distributions [3], such as the hybrid PCF considered in this work, and will therefore not be used.

By inserting Eq. (11) into Eq. (2), and Eqs. (8)–(10) into Eq. (3), expressions for all the terms in the wave equation, Eq. (1), are obtained. First, the pump field is considered, i.e. the terms oscillating at the pump frequency are collected. By inserting the aforementioned equations in Eq. (1), the terms oscillating at the pump frequency are:

$$\begin{aligned}&\mathbf{A}_1\frac{\partial^2}{\partial x^2}F_1(x,y)+\mathbf{A}_1\frac{\partial^2}{\partial y^2}F_1(x,y)-F_1(x,y)\beta_1^2\mathbf{A}_1+\frac{n^2\omega_1^2}{c^2}F_1(x,y)\mathbf{A}_1\\&+F_1(x,y)\frac{\partial^2}{\partial z^2}\mathbf{A}_1+2i\beta_1F_1(x,y)\frac{\partial}{\partial z}\mathbf{A}_1=\\&-\frac{\omega_1^2}{4c^2}\chi^{(3)}_{xxxx}F_1^2(x,y)F_1^*(x,y)\Big((\mathbf{A}_1\cdot\mathbf{A}_1)\mathbf{A}_1^*+2(\mathbf{A}_1^*\cdot\mathbf{A}_1)\mathbf{A}_1\Big)\,,\end{aligned}\tag{12}$$

The first four terms on the left-hand side of Eq. (12) are recognized as the solution to the linear wave equation, e.g. when nonlinear polarization is not considered, and these terms sum to zero. Eq. (12) thus reduces to:

$$\begin{aligned}&F_1(x,y)\frac{\partial^2}{\partial z^2}\mathbf{A}_1+2i\beta_1F_1(x,y)\frac{\partial}{\partial z}\mathbf{A}_1=\\&-\frac{\omega_1^2}{4c^2}\chi^{(3)}_{xxxx}F_1^2(x,y)F_1^*(x,y)\Big((\mathbf{A}_1\cdot\mathbf{A}_1)\mathbf{A}_1^*+2(\mathbf{A}_1^*\cdot\mathbf{A}_1)\mathbf{A}_1\Big)\,.\end{aligned}\tag{13}$$

Applying the slowly-varying envelope approximation, $\frac{\partial^2}{\partial z^2}\mathbf{A}_1 << \frac{\partial}{\partial z}\mathbf{A}_1$, replacing $\chi^{(3)}_{xxxx}$ with the nonlinear refractive index, $n_2=\frac{3}{8n}\chi^{(3)}_{xxxx}$, multiplying both sides with $F_1^*(x,y)$ and integrating over the transverse coordinates the following is obtained:

$$\frac{\partial}{\partial z}\mathbf{A}_1=\frac{i\omega_1 n_2}{3c}\frac{\iint_{-\infty}^{\infty}F_1^2(x,y)F_1^{*2}(x,y)dxdy}{\iint_{-\infty}^{\infty}F_1(x,y)F_1^*(x,y)dxdy}\Big((\mathbf{A}_1\cdot\mathbf{A}_1)\mathbf{A}_1^*+2(\mathbf{A}_1^*\cdot\mathbf{A}_1)\mathbf{A}_1\Big)\,.\tag{14}$$

A change of variable is applied such that $|\mathbf{A}_1|^2$ represents the optical power, by replacing $\mathbf{A}_1$ with $\mathbf{A}_1\sqrt{\frac{1}{2}\varepsilon_0 cn\iint_{-\infty}^{\infty}F_1(x,y)F_1^*(x,y)dxdy}$ and the nonlinear refractive index with $n_2\frac{2}{\varepsilon_0 cn}$:

$$\frac{\partial}{\partial z}\mathbf{A}_1=\frac{i\omega_1 n_2}{3c}\frac{\iint_{-\infty}^{\infty}F_1^2(x,y)F_1^{*2}(x,y)dxdy}{(\iint_{-\infty}^{\infty}F_1(x,y)F_1^*(x,y)dxdy)^2}\Big((\mathbf{A}_1\cdot\mathbf{A}_1)\mathbf{A}_1^*+2(\mathbf{A}_1^*\cdot\mathbf{A}_1)\mathbf{A}_1\Big)\,.\tag{15}$$

Eq. (15) describes the dynamic of the pump field in the FWM process in the undepleted pump regime. In the same manner the equations for the signal and idler can be derived:

$$\begin{aligned}\frac{\partial}{\partial z}\mathbf{A}_2=&\frac{2i\omega_2 n_2}{3c}\Bigg[f_{12}\Big((\mathbf{A}_1^*\cdot\mathbf{A}_1)\mathbf{A}_2+(\mathbf{A}_1^*\cdot\mathbf{A}_2)\mathbf{A}_1+(\mathbf{A}_1\cdot\mathbf{A}_2)\mathbf{A}_1^*\Big)+\\&f_{1132}\Big((\mathbf{A}_3^*\cdot\mathbf{A}_1)\mathbf{A}_1+\frac{1}{2}(\mathbf{A}_1\cdot\mathbf{A}_1)\mathbf{A}_3^*\Big)e^{-i\Delta\beta z}\Bigg]\,,\end{aligned}\tag{16}$$

$$\begin{aligned}\frac{\partial}{\partial z}\mathbf{A}_3=&\frac{2i\omega_2 n_2}{3c}\Bigg[f_{13}\Big((\mathbf{A}_1^*\cdot\mathbf{A}_1)\mathbf{A}_3+(\mathbf{A}_1^*\cdot\mathbf{A}_3)\mathbf{A}_1+(\mathbf{A}_1\cdot\mathbf{A}_3)\mathbf{A}_1^*\Big)+\\&f_{1123}\Big((\mathbf{A}_2^*\cdot\mathbf{A}_1)\mathbf{A}_1+\frac{1}{2}(\mathbf{A}_1\cdot\mathbf{A}_1)\mathbf{A}_2^*\Big)e^{-i\Delta\beta z}\Bigg]\,,\end{aligned}\tag{17}$$

#231607 - $15.00 USD Received 29 Dec 2014; revised 16 Feb 2015; accepted 17 Feb 2015; published 25 Feb 2015
© 2015 OSA

where the overlap integrals are defined as:

$$f_{jk} = \frac{\iint_{-\infty}^{\infty} F_j^* F_j F_k^* F_k dxdy}{\iint_{-\infty}^{\infty} F_j F_j^* dxdy \iint_{-\infty}^{\infty} F_k F_k^* dxdy} , \tag{18}$$

$$f_{ijkl} = \frac{\iint_{-\infty}^{\infty} F_i F_j F_k^* F_l^* dxdy}{\sqrt{\iint_{-\infty}^{\infty} F_i F_i^* dxdy \iint_{-\infty}^{\infty} F_j F_j^* dxdy \iint_{-\infty}^{\infty} F_k F_k^* dxdy \iint_{-\infty}^{\infty} F_l F_l^* dxdy}} . \tag{19}$$

The parametric gain can be calculated from Eqs. (15)–(17). In the following, two different cases are considered; signal and idler fields are generated with the same polarization state as the pump field, and signal and idler fields are generated with polarization states orthogonal to the polarization state of the pump field. The effective phase mismatch and parametric gain is derived in both cases.

3.1. Co-polarized pump, signal and idler fields

Firstly, a co-polarized pump, signal and idler field are considered. If it is assumed that the pump, signal and idler fields are all polarized along x, the Jones vector can be written:

$$\mathbf{A}_j = A_j \begin{pmatrix} \hat{e}_x \\ 0 \end{pmatrix} , \tag{20}$$

where $\hat{e}_x$ is the unit vector along x and $|A_j|^2$ is the optical power. By inserting Eq. 20 in Eqs. (15)–(17), following a similar approach as in [21], and assuming $\frac{n_2\omega_l}{c} \approx \frac{n_2\omega_1}{c}$ for $l = 2,3$, an expression for the effective phase mismatch, $\kappa_{||}$, and the parametric gain, $g_{||}$, can be obtained:

$$\kappa_{||} = \Delta\beta + 2\frac{n_2\omega_1}{c} P_p (f_{12} + f_{13} - f_{11}) , \tag{21}$$

$$g_{||} = \sqrt{\left(\frac{n_2\omega_1}{c} P_p f_{1123}\right)^2 - \left(\frac{\kappa_{||}}{2}\right)^2} , \tag{22}$$

where $P_p = |A_p(0)|^2$ is the pump power at $z = 0$.

3.2. Orthogonally polarized pump and signal and idler fields

In this case, a pump field orthogonally polarized to the signal and idler fields is considered. Assuming the pump field is x-polarized, the Jones vectors can be written:

$$\mathbf{A}_1 = A_1 \begin{pmatrix} \hat{e}_x \\ 0 \end{pmatrix} , \qquad \mathbf{A}_j = A_j \begin{pmatrix} 0 \\ \hat{e}_y \end{pmatrix} , \; j = 2,3 . \tag{23}$$

Again Eq. 23 is inserted in Eqs. (15)–(17), and by following a similar approach as in [21] and assuming $\frac{n_2\omega_l}{c} \approx \frac{n_2\omega_1}{c}$ for $l = 2,3$, an expression for the effective phase mismatch, $\kappa_{\perp}$, and the parametric gain, $g_{\perp}$, can be found for the pump field orthogonally polarized to the signal and idler fields:

$$\kappa_{\perp} = \Delta\beta + 2\frac{n_2\omega_1}{c} P_p (\frac{1}{3} f_{12} + \frac{1}{3} f_{13} - f_{11}) , \tag{24}$$

$$g_{\perp} = \sqrt{\left(\frac{n_2\omega_1}{3c} P_p f_{1123}\right)^2 - \left(\frac{\kappa_{\perp}}{2}\right)^2} , \tag{25}$$

where $P_p = |A_p(0)|^2$ is the pump power at $z = 0$.

Eqs. (21) and (24) can be simplified if the overlap integrals are approximated with $\frac{1}{A_{eff}}$, where A_{eff} is the effective mode area. Thereby the effective phase mismatches are given by:

#231607 - $15.00 USD Received 29 Dec 2014; revised 16 Feb 2015; accepted 17 Feb 2015; published 25 Feb 2015
© 2015 OSA

$\kappa_{\parallel,approx} = \Delta\beta + 2\frac{n_2\omega_1}{A_{eff}c}P_p$ and $\kappa_{\perp,approx} = \Delta\beta - \frac{2}{3}\frac{n_2\omega_1}{A_{eff}c}P_p$, in agreement with [22]. An interesting difference between the two cases is observed. For co-polarized pump, signal and idler fields, the nonlinear contribution to the effective phase mismatch is positive, for orthogonally polarized pump, signal and idler fields, the nonlinear contribution to the effective phase mismatch is negative. In the following, the field overlap integrals are used to calculate the parametric gain, since the $\frac{1}{A_{eff}}$-approximation does not apply to fibers with strongly frequency-dependent field distributions such as the hybrid PCFs.

4. Calculated parametric gain

The parametric gain of a degenerate FWM processes in the hybrid PCF is calculated for two cases; for signal and idler fields generated with same polarization states as the polarization state of the pump field, and for signal and idler fields generated in orthogonal polarization states with respect to the polarization state of the pump field. Eqs. (22) and (25) are used. A pump power of 25 kW and a pump wavelength of 1064 nm is used in the calculations. A value of 2.7×10^{-16} cm^2/W is used for the nonlinear index coefficient, n_2 [23].

In Fig. 5 the calculated parametric gain is shown. The gain is calculated for the pump in the FM polarized along the slow axis, Fig. 5(a) and Fig. 5(c), and for the pump in the FM polarized along the fast axis, Fig. 5(b) and Fig. 5(d), indicated in the figures with the arrow in the "Input" microscope image inset. The gain is calculated for the signal and idler being generated in the same mode, which is either one of the two polarizations of the FM, HOM11, or HOM12. The polarization of the generated FWM components is indicated with the arrow in the "Output" microscope image inset. The legend in the bottom right graph applies to all the graphs. A zoom at the FWM components generated in the HOM11 and HOM12 modes are shown in all graphs. A zoom of the FWM components generated in the FM polarized along the fast axis for an input pump polarized along the slow axis, which are observed in Fig. 5(a), is shown in Fig. 6(a).

Several narrow gain peaks are observed in Fig. 5. In all polarization combinations, intermodal FWM gain peaks are observed for signal and idler generated in HOM11 and HOM12. The position of these gain peaks differ for the different combinations, but the peaks are observed at 830 nm-850 nm and 1425 nm-1485 nm. The widths of the gain peaks are rather small, on the order of a few nm. The FWM components at 830 nm-850 nm lies well within the 4th bandgap, and the dispersion properties are not affected by the PBG effect, see Fig. 4(b). The HOM11 FWM components at 1425 nm-1485 nm lies well within the 2nd HOM11 bandgap, and the dispersion properties of these components are therefore neither affected by the PBG effect. The phase matching technique for HOM11 is thus based on intermodal phase matching. The dispersion properties of HOM12 in the 2nd HOM12 bandgap are affected by the PBG effect for wavelengths shorter than 1480 in the slow axis, and wavelengths shorter than 1470 nm in the fast axis, see Fig. 4(b). The phase matching for HOM12 is thus based on intermodal phase matching and phase matching by dispersion tailoring through the PBG effect in Fig. 5(a), 5(b) and 5(d). However, for the orthogonally polarized pump, signal and idler fields, with the pump polarized along the slow axis shown in Fig. 5(c), the dispersion properties of HOM12 are affected to a very small degree by the PBG effect.

The relative different spectral positions of the gain peaks can be explained by considering $\Delta\beta$. $\Delta\beta_y = \Delta\beta_x - \Delta n_2\frac{\omega_2}{c} - \Delta n_3\frac{\omega_3}{c} + 2\Delta n_1\frac{\omega_1}{c}$, where Δn_j, $j = 1,2,3$ are the birefringence at the signal, idler and pump wavelengths. If $\Delta\beta$ decreases for a given input- and output polarization state, the spectral distance from the pump to the generated FWM pair increases; the short wavelength FWM component is blue shifted, and the long wavelength FWM component is red shifted. In the co-polarized case, the spectral distance between the pump and the signal and idler generated in HOM11 is larger for FWM components generated in the slow axis, Fig. 5(a), compared to the FWM components generated in the fast axis, Fig. 5(d). Thus $-\Delta n_2\frac{\omega_2}{c} - \Delta n_3\frac{\omega_3}{c} + 2\Delta n_1\frac{\omega_1}{c} >$

#231607 - $15.00 USD Received 29 Dec 2014; revised 16 Feb 2015; accepted 17 Feb 2015; published 25 Feb 2015
© 2015 OSA

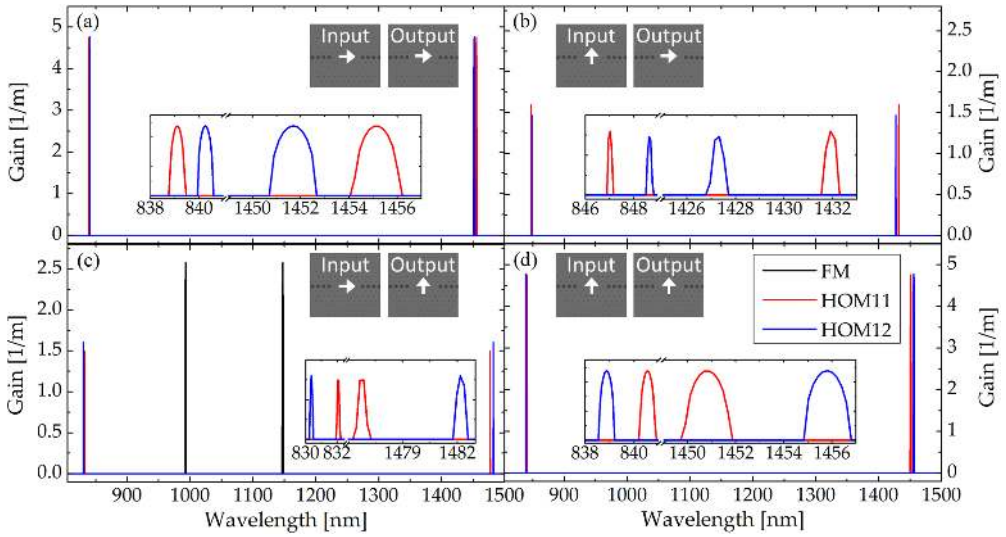

Fig. 5. Calculated parametric gain for co- and orthogonally polarized pump, signal and idler fields. The FM polarized along the slow and fast axis are considered as the pump mode, indicated with the arrow in the "Input" microscope image inset. A pump wavelength and power of respectively 1064 nm and 25 kW is used. The parametric gain for signal and idler generated in the FM, HOM11, and HOM12 is calculated, the polarization states of the FWM components are indicated with the arrow in the "Output" microscope image inset. The legend in the bottom right graph applies to all the graphs.

0. For the co-polarized case with signal and idler generated in HOM12 the situation is the opposite, the spectral distance between the pump and the signal and idler is larger for FWM components generated in the fast axis, Fig. 5(d), compared to the FWM components generated in the slow axis, Fig. 5(a). Thus $-\Delta n_2 \frac{\omega_2}{c} - \Delta n_3 \frac{\omega_3}{c} + 2\Delta n_1 \frac{\omega_1}{c} < 0$. Δn_2 and Δn_3 are much higher for HOM12 than for HOM11, since HOM12 are affected by the stress induced birefringence to a larger degree than HOM11, see Fig. 4(c), which supports the observed behaviour. For orthogonally polarized pump, signal and idler, the spectral distance between pump and signal and idler generated in both HOM11 and HOM12 is larger for the pump polarized along the slow axis, Fig. 5(c), than for the pump polarized along the fast axis, Fig. 5(b). Thus $-\Delta n_2 \frac{\omega_2}{c} - \Delta n_3 \frac{\omega_3}{c} + 2\Delta n_1 \frac{\omega_1}{c} > 0$ in both cases.

Intramodal FWM, where the signal and idler are generated in the FM, is only observed for orthogonally polarized pump, signal and idler fields, with the pump polarization along the slow axis as shown in Fig. 5(c). The parametric gain for the intramodal FWM is 1.6 times larger than the gain for the intermodal FWM, where the signal and idler are generated in the LP_{11} modes, for the same input and output polarization states. In general, the gain is largest for co-polarized pump, signal and idler configuration, as predicted by Eqs. (22) and (25).

In practice, the gain peaks may be broader and of lower magnitude than observed in Fig. 5. Small fluctuations in the physical dimensions of the fabricated hybrid PCF in the longitudinal direction of the fiber may alter the phase matching criteria, and thus the spectral position of the maximum of the parametric gain can change slightly throughout the length of the hybrid PCF.

#231607 - $15.00 USD Received 29 Dec 2014; revised 16 Feb 2015; accepted 17 Feb 2015; published 25 Feb 2015
© 2015 OSA

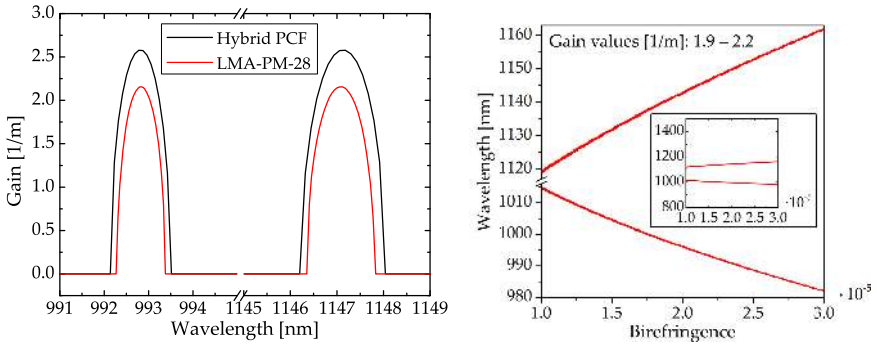

(a) (b)

Fig. 6. (a) Calculated parametric gain in the hybrid photonic crystal fiber (PCF) for orthogonally polarized pump, signal, and idler fields, all in the fundamental mode. The pump is polarized along the slow axis, and the signal and idler are polarized along the fast axis. The parametric gain of a simulated large mode area (LMA) polarization maintaining (PM) fiber with a core diameter of 28 µm and birefringence of 2.21×10^{-5} is also shown for orthogonally polarized pump, signal and idler. A pump wavelength and power of 1064 nm and 25 kW, respectively, are used in both cases. **(b)** Calculated maximum parametric gain in a simulated LMA PM fiber with a mode field diameter of 28 µm for a pump wavelength of 1064 nm and a pump power of 25 kW. The gain values lies in the range 1.9 m^{-1} and 2.2 m^{-1}. The mode refractive indices are calculated by the Sellmeier equation, a constant offset corresponding to the birefringence is used in the fast axis.

4.1. Comparison with a simulated polarization maintaining large mode area fiber

The birefringence assisted phase matching in the hybrid PCF can be compared with the phase matching in a LMA PM fiber with no PBG elements. For this purpose a simulated LMA PM fiber with MFD 28 µm (LMA-PM-28) is considered. The waveguide dispersion in a LMA-PM-28 is small compared to the material dispersion, so it is assumed, that the dispersion properties are the same as for bulk silica. The mode indices of the slow and fast axis are calculated from the Sellmeier equation for fused silica, but a negative constant offset is introduced in the fast axis to represent birefringence. The parametric gain of birefringence assisted FWM in the LMA-PM-28 is calculated for a pump wavelength of 1064 nm and a pump power of 25 kW for a range of birefringence values between 1×10^{-5} and 3×10^{-5} in steps of 1×10^{-7}. The calculated maximum gain varies between 1.9 m^{-1} and 2.2 m^{-1} for the considered range of birefringence values and the spectral widths of the gain peaks are less than 2 nm. The spectral location of the maximum gain is shown in Fig. 6(b). The pump is polarized along the slow axis, and the signal and idler are orthogonally polarized along the fast axis. The phase matching in the full spectral range of 800 nm to 1500 nm is shown in the inset of the figure.

As shown in Fig. 6(b), the phase matched wavelengths are very sensitive to the birefringence. For values between 1×10^{-5} and 3×10^{-5} the phase matched wavelengths are shifted from 1015 nm and 1119 nm to 982 nm and 1162 nm. In Fig. 6(a) the parametric gain of the LMA-PM-28 with a birefringence of 2.21×10^{-5} is compared to the intramodal parametric gain of the hybrid PCF for orthogonally polarized pump, signal and idler, with the pump polarized along the slow axis. The birefringence of the hybrid PCF is 2.12×10^{-5} at 1064 nm. The gain is slightly higher in the hybrid PCF, but the spectral positions of the gain peaks are identical. This comparison underlines that the intramodal FWM is due to birefringence assisted phase matching in the hybrid PCF. Note that the parametric gain of the simulated LMA-PM-28 is

#231607 - $15.00 USD Received 29 Dec 2014; revised 16 Feb 2015; accepted 17 Feb 2015; published 25 Feb 2015
© 2015 OSA

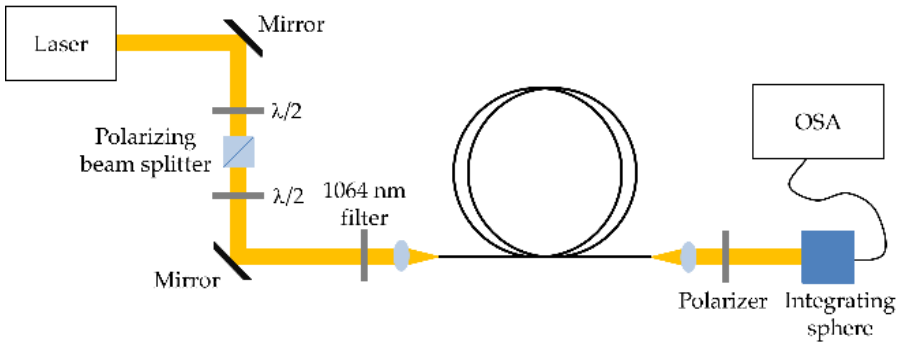

Fig. 7. Schematic illustration of the measurement setup. A linearly polarized Ytterbium-doped 40 ps 1064 nm fiber laser with repetition rate of 1 MHz is launched in the hybrid photonic crystal fiber through two half-wave plates, $\lambda/2$, a polarizing beam splitter, and a 1064 nm laser line filter. The fiber output is collected in an integrating sphere through a polarizer.

zero in the spectral regions 830 nm-850 nm and 1425 nm-1485 nm, where intermodal FWM is observed.

5. Measurements

In Fig. 7 a schematic illustration of the measurement setup is shown. A linearly polarized Ytterbium-doped 40 ps 1064 nm fiber laser with a repetition rate of 1 MHz is used as pump laser. To ensure stable laser performance the average output power of the laser is fixed, and a half-wave plate, $\lambda/2$, and a polarizing beam splitter is used to adjust the input power. Another half-wave plate, $\lambda/2$, is used to adjust the polarization along the principal axes of the hybrid PCF. A 1064 nm laser line filter is inserted before the fiber input to avoid spontaneous emission from the laser.

On the output side of the fiber a polarizer is inserted to measure the light polarized along the Ge-doped rods and the light polarized orthogonally to the Ge-rods. In practice the polarizations are separated by a polarizing beam splitter. The light is collected by an integrating sphere connected to an optical spectrum analyzer (OSA) through a multimode fiber with core diameter 100 μm. Two lengths of the hybrid PCF are considered, 2 m and 6 m. The hybrid PCFs are coiled with a diameter of approximately 50 cm.

5.1. Spontaneous degenerate four-wave mixing

In Figs. 8(a) and 8(b) the output spectra of the hybrid PCFs of respectively 2 m and 6 m are shown for different pump peak powers. The pump laser is launched in the FM of the hybrid PCF, polarized along the slow axis or the fast axis. The input polarization is indicated in the figures with the arrow in the "Input" microscope image inset. The output spectra of the two principal axes of the fibers have been collected. The polarization of the collected spectra is indicated with the arrow in the "Output" microscope image inset. Note that the spectral component at 1064 nm observed in the spectra of orthogonal output polarization with respect to that of the input pump polarization stems from cross-coupling between the two polarizations. The pump peak powers are stated in the legends, and the legends shown in the bottom graphs also applies to the graph right on top of those, which have the same polarization input state.

In Fig. 9(a) an image of the output from the 2 m long hybrid PCF with an input peak power

#231607 - $15.00 USD Received 29 Dec 2014; revised 16 Feb 2015; accepted 17 Feb 2015; published 25 Feb 2015
© 2015 OSA

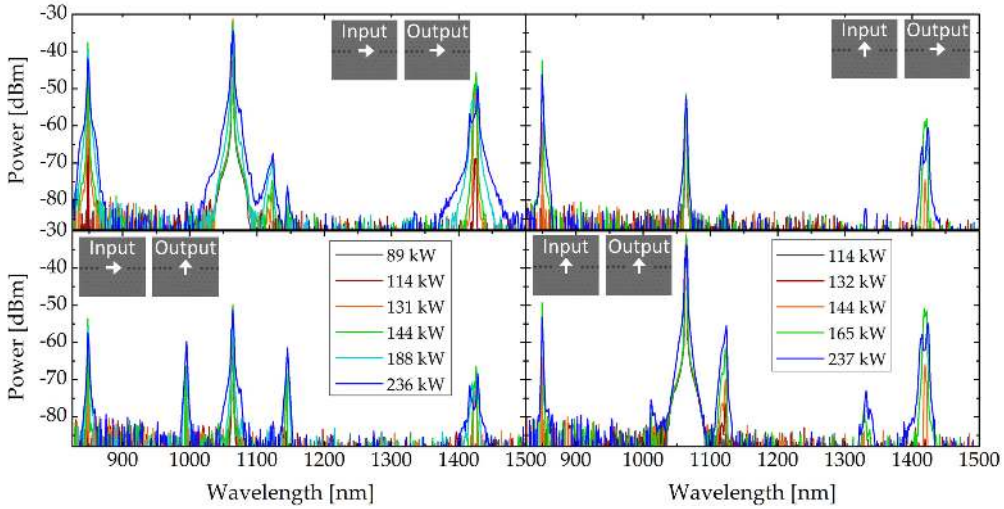

(a) 2 m.

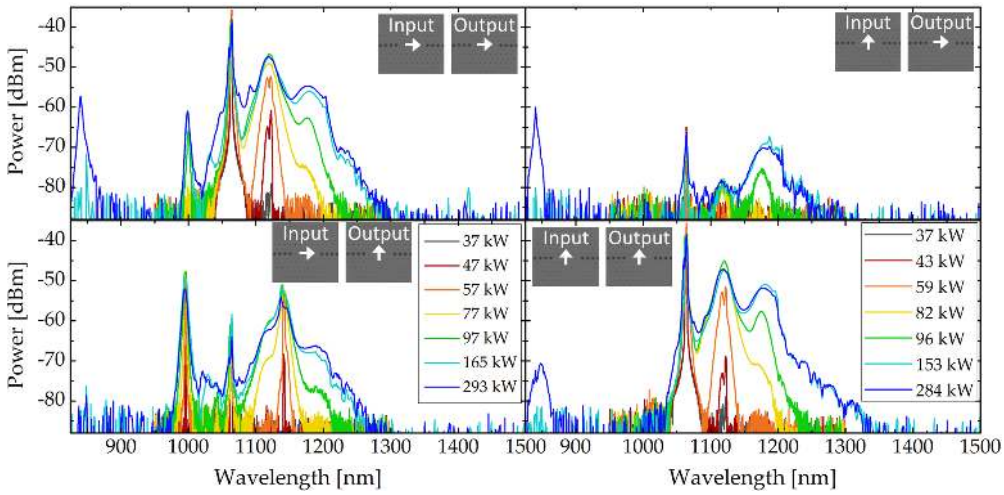

(b) 6 m.

Fig. 8. Output spectra of the hybrid photonic crystal fiber for different pump peak powers. The pump polarization state is indicated with the arrow in the "Input" microscope image inset. The output polarization state is indicated with the arrow in the "Output" microscope image inset. The pump peak powers are stated in the legends, the legends shown in the bottom graphs also applies to the graphs of same polarization input state.

of 210 kW is shown. The output is divided spatially, by propagating the output through a prism, and the components are imaged onto an IR-card. Furthermore, images of the modes at 995 nm and 1145 nm are shown in Figs. 9(b) and 9(c), respectively. These images were achieved by imaging the hybrid PCF output onto a black and white CCD camera through a narrow spectral filter.

In Figs. 10(a)–10(d) the average output power with respect to the average input power is shown in the 2 m and 6 m length of hybrid PCF for a pump input polarization along the slow axis and the fast axis. The total output power and the power in each of the principal fiber axes are

#231607 - $15.00 USD Received 29 Dec 2014; revised 16 Feb 2015; accepted 17 Feb 2015; published 25 Feb 2015
© 2015 OSA

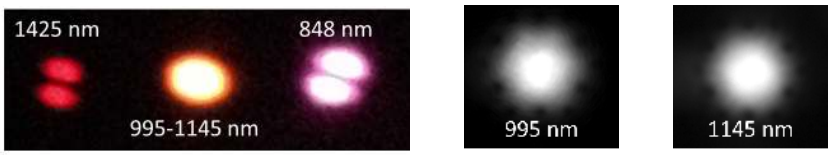

(a) (b) (c)

Fig. 9. Output from the 2 m long hybrid PCF with an input peak power of 210 kW. The wavelengths of the imaged modes are stated in the figures. In (a) the output is divided spatially through a prism, the components are imaged onto an IR-card. In (b) and (c) the output is imaged onto a black and white CCD camera through a narrow spectral filter.

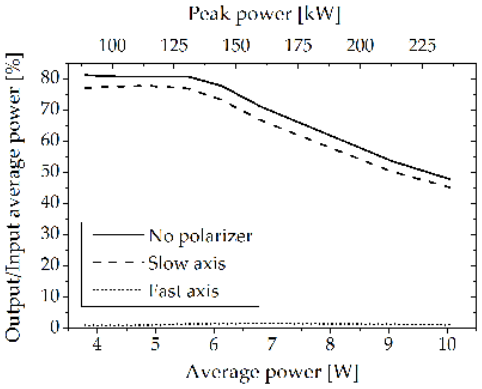

(a) 2 m, pump polarized along slow axis.

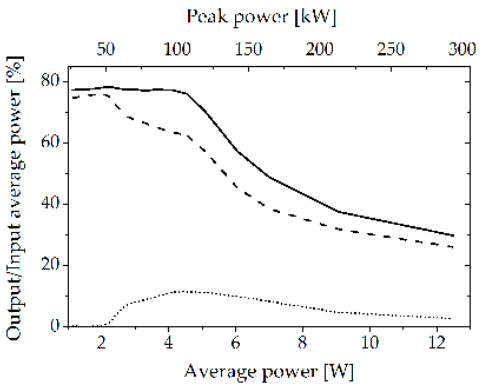

(b) 6 m, pump polarized along slow axis.

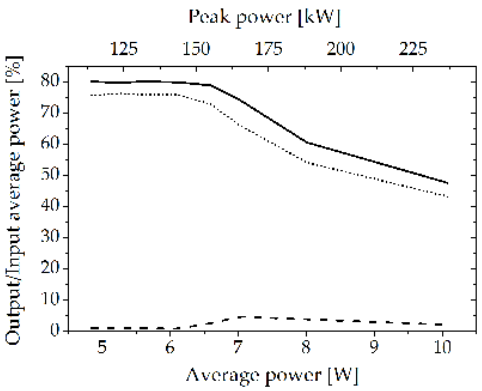

(c) 2 m, pump polarized along fast axis.

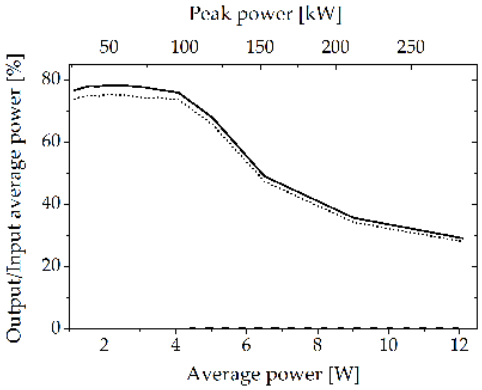

(d) 6 m, pump polarized along fast axis.

Fig. 10. Average output power with respect to the average input power of the hybrid photonic crystal fiber. The total output power and the power in each of the principal fiber axes, the slow and fast axis, are shown. The fiber length and pump polarization are stated under each graph.

shown. For low input powers the relationship between the output and input power corresponds to the coupling efficiency.

Different spectral components are observed in Fig. 8. Raman scattering is observed at the first Stokes wave at approximately 1120 nm in the same output polarization as the input polar-

#231607 - $15.00 USD Received 29 Dec 2014; revised 16 Feb 2015; accepted 17 Feb 2015; published 25 Feb 2015
© 2015 OSA

ization in the 2 m length of hybrid PCF and in the 6 m length of hybrid PCF. The Raman threshold is substantially lower in the 6 m PCF, and thus a larger amount is observed in the longer fiber. Furthermore, Raman scattering is observed at the second Stokes wave at approximately 1180 nm in the longer fiber. Raman scattering is also observed in the polarization orthogonal to the input polarization in the longer fiber, but of much lower magnitude. This is attributed to cross-coupling between the two principal fiber axes, since the Raman gain is substantially lower for orthogonally polarized pump and Stokes waves [21].

Intermodal FWM between the pump in the FM and the signal and idler in the LP_{11} mode is observed at 848 nm and 1425 nm in Fig. 8(a) in good agreement with the calculated parametric gain. The relative difference between the spectral locations of the calculated and experimentally observed FWM components is less than 4 % for all considered polarization state combinations. The 848 nm component is also visible for three of the configurations in Fig. 8(b) at high pump powers. Loss is expected for the LP_{11} mode, and the output average power with respect to the input average power decreases for higher pump peak powers, both in the 2 m and 6 m long fiber, after the onset of the intermodal FWM as observed in Fig. 10. For the highest pump power the output average power with respect to the input average power is less than 30 % in the 6 m hybrid PCF for the pump polarized along the slow and the fast axis as shown in Fig. 10(b) and 10(d). This loss is due to intermodal FWM in the lossy LP_{11} mode. For a pump peak power of approximately 150 kW the intermodal FWM at 848 nm and 1425 nm are clearly observed in the 2 m long hybrid PCF as shown in Fig. 8(a), but they are not observed in the 6 m long hybrid PCF as shown in Fig. 8(b) due to this loss. The intermodal FWM occurs across bandgaps, the pump wavelength is located in the 3rd bandgap, while the 848 nm component lies in the 4th bandgap and the 1425 nm component lies in the 2nd bandgap.

For the pump polarized along the slow axis, birefringence assisted intramodal FWM, where the signal and idler are generated in the FM polarized along the fast axis, is observed in the 3rd bandgap for both hybrid PCF lengths. The FWM components are generated at 995 nm and 1145 nm in this process, in good agreement with the calculated parametric gain. The relative difference between the spectral locations of the calculated and experimentally observed intramodal FWM components is less than 1 %. In the 6 m long hybrid PCF the 995 nm and 1145 nm components are also observed in the output polarized along the slow axis, note that the 1145 nm component falls within the same spectral region as the Raman scattering. However, the magnitude is much smaller for the output polarized along the slow axis compared to the output polarized along the fast axis, and the intramodal FWM components observed in this polarization are attributed to cross-coupling between the two polarizations. In Fig. 10(b) a relative large amount of power arising in the fast axis for peak powers above 50 kW is observed. This is the power arising in the intramodal FWM components.

5.2. Generation efficiency of 848 nm

In the 2 m long hybrid PCF a fairly strong generation of light at 848 nm is observed for co-polarized pump, signal and idler, with the pump polarized along the slow axis. The generation efficiency of the 848 nm component is measured in the 2 m fiber piece, by positioning the fiber in a half-coil instead of the fully coiled fiber considered in Fig. 8(a), to decrease the bend loss at 848 nm. The FWM components are divided spatially through a prism, as in Fig. 9(a). Thereby it is possible to measure the power of the 848 nm component only, by physically blocking the other components.

In Fig. 11 the conversion efficiency of the 848 nm component is shown, given by average output power at 848 nm measured after the prism, divided by the pump laser average input power measured right after the 1064 nm filter, see Fig. 7. The conversion efficiency is maximum for an input peak power of 165 kW. The maximum conversion efficiency is given by 17.3 %, corre-

#231607 - $15.00 USD Received 29 Dec 2014; revised 16 Feb 2015; accepted 17 Feb 2015; published 25 Feb 2015
© 2015 OSA

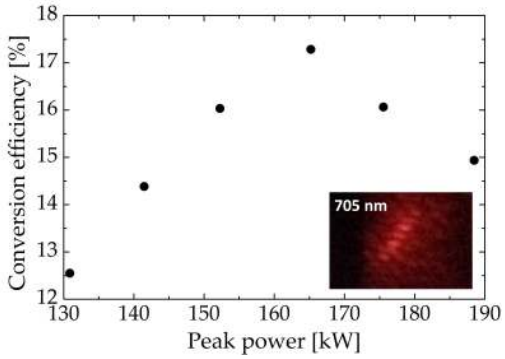

Fig. 11. Conversion efficiency of the 848 nm component given by average output power at 848 nm with respect to the average input power of the pump laser. Cascaded four-wave mixing is observed for pump peak powers beyound 165 kW giving rise to light generation at 705 nm. An image of the mode at 705 nm is shown in the inset.

sponding to an average output power of 1.2 W at 848 nm. The conversion efficiency decreases for input powers beyond 165 kW, since cascaded FWM sets in. Light at 705 nm was observed at higher power levels, an image of the fiber output at this wavelength is shown in the inset of Fig. 11. The 848 nm component acted as a pump for input powers beyond 165 kW for a FWM process generating FWM components at 1064 nm and 705 nm. The mode at 705 nm is very lossy, and a red glow from the fiber cladding in the longitudinal direction could be observed with the naked eye.

6. Conclusion

Degenerate FWM in a LMA hybrid PCF has been considered. Expressions of the effective phase mismatch and the parametric gain has been derived for co- and orthogonally polarized pump, signal and idler, which were used to calculate the parametric gain in the hybrid PCF. Intramodal birefringence assisted phase matching and intermodal phase matching were observed. The parametric gain of a simulated PM LMA fiber with a MFD of 28 μm was also calculated, by assuming the refractive mode indices of the slow and fast axis were given by the Sellmeier equation, however, a negative offset corresponding to the fiber birefringence was introduced in the fast axis. Similar spectral positions of the parametric gain were obtained in the hybrid PCF and the simulated LMA fiber of similar birefringence, underlining that the intramodel FWM observed in the hybrid PCF relies on birefringence assisted phase matching.

Spontaneous degenerate FWM was measured in 2 m and 6 m lengths of hybrid PCF for a linearly polarized pump at 1064 nm. The FWM processes for co- and orthogonally polarized pump, signal and idler were considered. Intramodal birefringence assisted phase matching and intermodal phasematching were observed in good agreement with the numerical results. The conversion efficiency of the intermodal FWM process was measured for the short wavelength component, and a conversion efficiency of 17 % was obtained. This work characterizes the different phase matching techniques in the hybrid PCF, and demonstrates the potential of using LMA hybrid PCFs to extend the spectral coverage of high power fiber light sources.

#231607 - $15.00 USD Received 29 Dec 2014; revised 16 Feb 2015; accepted 17 Feb 2015; published 25 Feb 2015
© 2015 OSA